Front. Earth Sci. 2019, 13(4): 791–807
https://doi.org/10.1007/s11707-019-0799-z

RESEARCH ARTICLE

On the rapid intensification for Typhoon Meranti (2016): convection, warm core, and heating budget

Xiba TANG[1,2], Fan PING (✉)[1], Shuai YANG (✉)[1], Mengxia LI[3], Jing PENG[4]

1 Laboratory of Cloud-Precipitation Physics and Severe Storms, Institute of Atmospheric Physics, Chinese Academy of Sciences, Beijing 100029, China
2 Plateau Atmosphere and Environment Key Laboratory of Sichuan Province, Chengdu 610225, China
3 China Meteorological Administration Henan Key Laboratory of Agrometeorological Support and Applied Technique, Zhengzhou 450000, China
4 Key Laboratory of Regional Climate-Environment for Temperate East Asia, Institute of Atmospheric Physics, Chinese Academy of Sciences, Beijing 100029, China

Abstract Through a cloud-resolving simulation of the rapid intensification (RI) of Typhoon Meranti (2016), the convections, warm core, and heating budget are investigated during the process of RI. By investigating the spatial distributions and temporal evolutions of both convective-stratiform precipitation and shallow-deep convections, we find that the inner-core convections take mode turns, from stratiform-precipitation (SP) dominance to convective-precipitation (CP) prevalence during the transition stages between pre-RI and RI. For the CP, it experiences fewer convections before RI, and the conversion from moderate/moderate-deep convections to moderate-deep/deep convections during RI. There is a clear upper-level warm-core structure during the process of RI. However, the mid-low-level warming begins first, before the RI of Meranti. By calculating the local potential temperature (θ) budget of various convections, the link between convections and the warm core (and further to RI via the pressure drop due to the warming core) is established. Also, the transport pathways of heating toward the center of Meranti driven by pressure are illuminated. The total hydrostatic pressure decline is determined by the mid-low-level warm anomaly before RI, mostly caused by SP. The azimuthal-mean diabatic heating is the largest heating source, the mean vertical heat advection controls the vertical downwards transport by adiabatic warming of compensating downdrafts above eye region, and then the radial θ advection term radially transports heat toward the center of Meranti in a slantwise direction. Accompanying the onset of RI, the heating efficiency of the upper-level warming core rises swiftly and overruns that of the mid-low-level warm anomaly, dominating the total pressure decrease and being mainly led by moderate-deep and deep convections. Aside from the characteristics in common with SP, for CP, the eddy component of radial advection also plays a positive role in warming the core, which enhances the centripetal transport effect and accelerates the RI of Meranti.

Keywords convection, upper-level warm core, heating budget, Typhoon Meranti, tropical cyclone

1 Introduction

In the past 30 years, significant progress has been made in the prediction of tropical cyclone (TC) tracks, but the forecasting of TC intensity still faces a greater challenge. In particular, for TCs that experience rapid intensification (RI), it is more difficult to predict their sudden intensity changes, and false reports or omissions often occur (DeMaria et al., 2014). Multi-scale interactions, including the environment, vortex, convection, turbulence, and microscales (Marks and Shay, 1998), reinforce the complexity of performing intensity forecasts, and thus it is still a challenging task at present.

Environmental conditions influencing the process of RI for TCs include warm sea surface temperature (SST), high ocean heat content, low vertical wind shear, high relative humidity in the lower troposphere, and strong upper-tropospheric outflow (Kaplan and DeMaria, 2003; Wang and Wu, 2004; Lin et al., 2008). However, Hendricks et al. (2010) made a global data set analyses and found no significant differences between environmental parameters for TCs undergoing RI versus those intensifying but at a lesser rate, indicating that the external conditions are only

Received March 31, 2019; accepted October 8, 2019

E-mails: pingf@mail.iap.ac.cn (Fan PING); yangs@mail.iap.ac.cn (Shuai YANG)

part of the picture with respect to the RI of TCs. In other words, inner-core processes operating at finer scales might also be important factors responsible for RI.

Several observational studies have found that RI is closely associated with abrupt increases in the number convections (or convective bursts, CBs) in the inner core (Reasor et al., 2009; Guimond et al., 2010; Molinari and Vollaro, 2010; Nguyen and Molinari, 2012; Rogers et al., 2015). Based on a composite analysis of airborne Doppler observations, Rogers et al. (2015) found that the RI of TCs involves a relatively large amount of CBs inside the radius of maximum wind (RMW) compared with steady-state TCs. Heymsfield et al. (2001) showed that the relationship between CBs and RI can generally be linked to enhanced latent heat release and subsidence in the storm core. Also, some recent modelling studies have emphasized the importance of the upper-level warming core in RI (Zhang and Chen, 2012; Chen and Zhang, 2013); specifically, the formation of an upper-level warm core, from the subsidence of stratospheric air associated with the detrainment of CBs, coincides with the onset of RI.

Because of this significance of the inner-core processes, especially on convections and aspects of warm-core evolution, more attention should be paid to analyze these processes in specific typhoon cases, which is what we aim to do here in this paper with respect to Typhoon Meranti (2016). Three questions will be addressed: 1) what are the spatial and temporal features of the various convections and warm-core structure during the RI process of Typhoon Meranti? 2) Can we differentiate between the contributions of the various convections to the heating of the warm core by calculating the local potential temperature (θ) budget, and 3) further quantify their effects on RI is driven by the central pressure drop? We attempt to answer these questions by employing a 120-h model simulation, as presented in Li et al. (2019). The next section provides an overview of Meranti. Sections 3 and 4 describe the vortex-scale evolution of Meranti and the distribution of different types of convections before and during RI. The importance of the warming core in determining the RI of Meranti in terms of pressure drops is discussed in Section 5. Local heat budgets for the various convections are analyzed in Section 6. A summary of our findings is provided in the final Section.

2 Case description and model configuration

2.1 General description of Meranti

Meranti formed as a tropical storm over the western North Pacific at 0600 UTC 10 September 2016. Then, it gradually intensified along with its north-westward movement (Fig. 1(a)). From 0000 UTC 11 September (Fig. 1 (b)), it experienced a period of RI, based on the broadly accepted definition of a maximum sustained 10-m wind increase of more than 15 m/s in 24 h (Kaplan and DeMaria, 2003). On 12 September, Meranti evolved into a super typhoon as it crossed the Luzon Strait. Ultimately, it reached peak intensity on 13 September. Shortly afterwards, Meranti passed to the south of Taiwan as a super typhoon, and made landfall at Xiamen, Fujian, at 1905 UTC 14 September, with a wind speed up to 48 m/s and a minimum central pressure of 945 hPa, causing 45 casualties and economic losses of more than US$ 4.76 billion (CMA, 2016).

2.2 Model setup

By utilizing the Weather Research and Forecasting model, Typhoon Meranti (2016) was successfully numerically simulated based on a two-way nested setup, with 9/3-km grid meshes and 32 vertical levels (Li et al., 2019). The integration ran from 0000 UTC 10 to 0000 UTC 15 September 2016, encompassing the lifecycle of Meranti's evolution and RI. The main model parameters are illustrated in Table 1. Readers have referred to Li et al. (2019) for more details on the model configuration used in this study. The outputs from the inner-domain simulation with the 3-km horizontal resolution are utilized to perform the analysis.

Figure 1 presents the simulated track and intensity of Typhoon Meranti, and then further detail in terms of the error against observation is provided in Table 2. The results show that the average error of the predicted TC path is 58.0 km. For the minimum sea-level pressure and the maximum sustained 10-m wind (MSW), the deviations of the predictions are no more than 4.3 hPa and 6.8 m/s, respectively, which is superior to the statistical data of 120-h intensity prediction for typhoons in the western Pacific reported by DeMaria et al. (2014), in which the mean MSW error reached 22 kt, which is approximately 11.3 m/s.

3 Vortex-scale features

Radius-height plots of azimuthally averaged vortex-scale features before and during the RI of Meranti are shown in Fig. 2. At 1200 UTC 10 September, the azimuthally averaged radial wind ($\overline{u}_r$, isoline in Fig. 2(a)) shows weak inflow of 3 m/s below the lowest 1-km layer and outflow (about 2–5 m/s) above 12 km. The weak tangential wind ($\overline{u}_t$, shaded in Fig. 2(a)) with a peak of 16 m/s is located at the top of the inflow layer, about 20 km from the center of the TC. The azimuthally averaged vertical velocity ($\overline{w}$, contoured in Fig. 2(b)) is mainly distributed between the radii of 48 and 72 km, with an intensity of > 0.6 m/s. After 12 h (Fig. 2(c)), the process of RI begins, accompanied by a markedly strengthened tangential wind (cf. the broad area of $\overline{u}_t > 24$ m/s below the height of 5 km, between the radii of 19 and 96 km) and lower-level inflow of nearly 7 m/s.

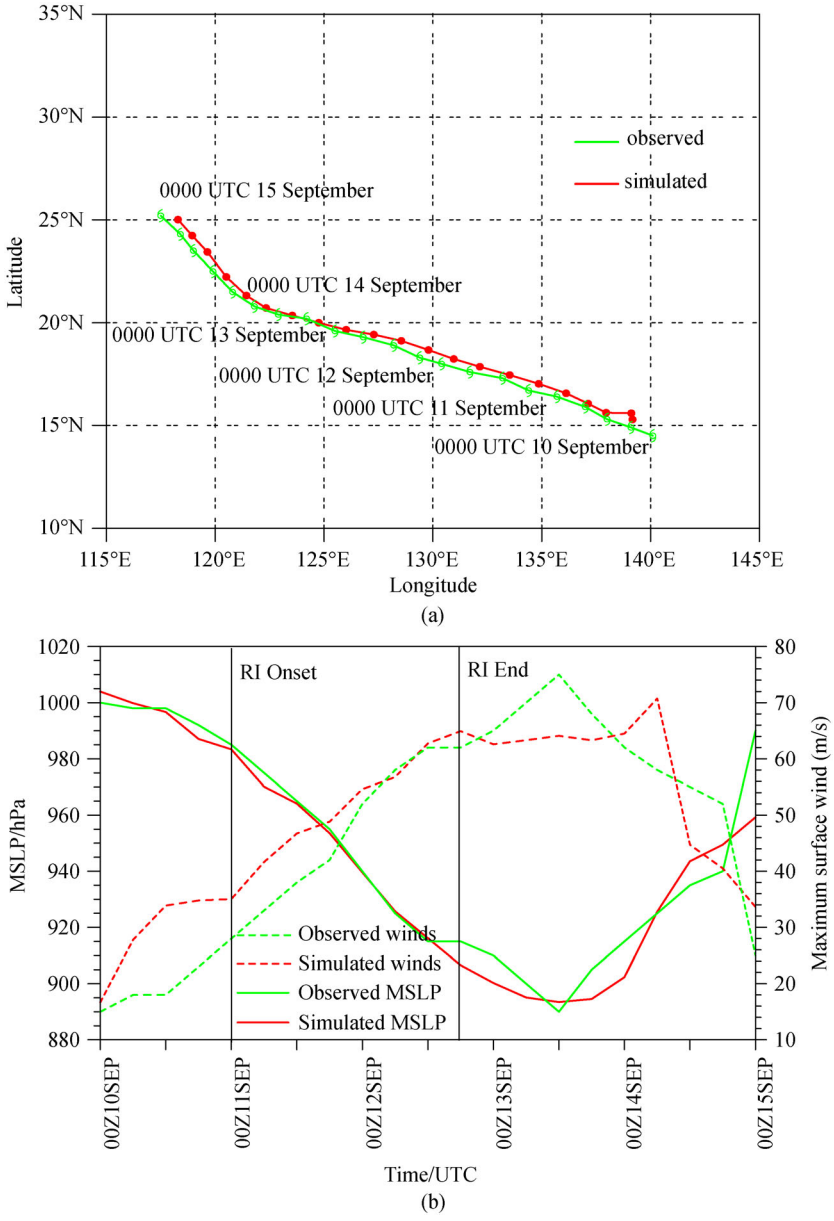

Fig. 1 (a) Best-track position according to China Meteorological Administration data (green line) and the position of Meranti simulated by WRF at 6-h intervals from 0000 UTC 10 September to 0000 UTC 15 September. (b) Mean sea level pressure (MSLP, solid lines) and maximum sustained 10-m wind (dashed lines) from 0000 UTC 10 September to 0000 UTC 15 September 2016. Best-track (simulated) values are shown as green (red) lines.

Table 1 Main model setup

	Domain 1	Domain 2
Horizontal grids	421 × 301	961 × 541
Grid spacing	9 km	3 km
Microphysical scheme	Goddard GCE	Goddard GCE
Cumulus scheme	Kain-Fritsch	None
Planetary boundary scheme	YSU	YSU
Land surface scheme	Noah	Noah
Longwave transfer scheme	RRTM	RRTM
Shortwave transfer scheme	Dudhia	Dudhia

The depth of the vortex ($\overline{\zeta}$, shaded in Fig. 2(d)) and updrafts increase and develop radially toward the center. Up until 1200 UTC 11 September (Fig. 2(e)), the vertical extent of the 24-m/s tangential wind contour keeps increasing from the altitude of 5 km at 0000 UTC to nearly 11 km at 1200 UTC 11 September, due to the RI of Meranti. The vorticity stretches vertically (Fig. 2(f)), with the maximum at the TC center, consistent with the result reported by Rogers (2010). The convections reach an intensity level of >1.6 m/s at the radius of 36 km and altitude of about 8–11 km, above the tangential wind peak. From Fig. 2, the lower-layer inflow increases abruptly and

Table 2 Forecast errors of path, minimum sea level pressure (MSLP), and maximum sustained 10-m wind (MSW) for Typhoon Meranti

Time (hh UTC dd Mon)	Predicted path error /km	MSLP error /hPa	MSW error /(m·s^{-1})
00 UTC 10 Sept	134.2	4.0	1.7
06 UTC 10 Sept	76.4	1.8	9.8
12 UTC 10 Sept	35.3	−1.3	15.9
18 UTC 10 Sept	22.8	−4.9	11.8
00 UTC 11 Sept	49.7	−1.6	7.0
06 UTC 11 Sept	62.1	−4.9	8.6
12 UTC 11 Sept	39.9	−0.9	8.7
18 UTC 11 Sept	57.8	−1.4	6.8
00 UTC 12 Sept	66.6	−0.4	2.6
06 UTC 12 Sept	60.2	0.7	−1.3
12 UTC 12 Sept	45.5	1.1	0.7
18 UTC 12 Sept	55.2	−8.4	2.9
00 UTC 13 Sept	56.9	−9.8	−2.4
06 UTC 13 Sept	64.8	−4.9	−6.7
12 UTC 13 Sept	70.5	3.5	−10.9
18 UTC 13 Sept	59.6	−10.4	−4.7
00 UTC 14 Sept	72.1	−12.6	2.5
06 UTC 14 Sept	73.0	0.6	12.7
12 UTC 14 Sept	71.0	8.5	−10.3
18 UTC 14 Sept	60.2	9.5	−11.5
00 UTC 15 Sept	89.4	−30.7	8.6

the eyewall convections develop radially and stretch upwards, which are possible precursor signals for the onset of Meranti's RI.

To clarify the lower-layer evolution of the wind field, Fig. 3 presents time-radius plots at the altitude of 0.25 km. The tangential wind strengthens swiftly from the pre-RI to the RI stage, and then increases from 24 m/s at the onset of RI to 40 m/s in a short time (Fig. 3(a)). Note that the RMW averages about 30-km during the RI. Figure 3(b) plots the azimuthally averaged reflectivity at the altitude of 3 km and the vertical velocity averaged in the 0.25-, 1- and 2-km layers. A band of enhanced low-level upward motion develops around 1200 UTC 10 September along the inner edge of the reflectivity peak. Before and during RI, the low-level upward motion is basically maintained at the radius of 72 km. So, this radius serves as an estimate of the inner-core size (Rogers, 2010), which is 2–3 times of the averaged RMW (Wang 2009; Li and Wang 2012).

4 Convection distributions: convective-stratiform precipitation and shallow-deep convections

To illuminate the detailed structure of the convective activities near the eyewall of Typhoon Meranti, the convective-stratiform spatial distributions are presented in Fig. 4. The horizontal charts of radar reflectivity, storm-relative flow vectors at the height of 3 km, and sea level pressure for three different stages of TC development are also plotted in the figure. In terms of the method used to partition the various convections, we take two steps. First, the whole inner-core region is separated into 'convective', 'stratiform', and 'other' types according to reflectivity values at the altitude of 3 km (R_3), based on the algorithm presented in Steiner et al. (1995), which has been widely used (e.g., Huang et al., 2019; Han et al., 2019; Zheng et al., 2019). The partitioning separates regions into 'convective' and 'stratiform' regions as follows: If $R_3 > 40$ dBZ, it is considered 'convective'; if 20 dBZ $< R_3 < 40$ dBZ, it is flagged as 'stratiform'; otherwise, it is classified as 'other'. After the first partitioning step, we further divide the convective precipitation (CP) into finer types based on the height of the cloud top (Tao and Jiang, 2015): shallow convection (SC) (height $\leqslant$ 6 km); moderate convection (MC) (6 km $<$ height $\leqslant$ 10 km); moderate-deep convection (MDC) (10 km $<$ height $\leqslant$ 14 km); and deep convection (DC) (height $>$ 14 km). The cloud top is represented by the 20-dBZ echo top if the maximum reflectivity in a column is no less than 20 dBZ. Note that, we also plot the various convections by partitioning algorithm from Rogers (2010) and from Steiner et al. (1995) (figure omitted). The main difference between them is CP-type distribution. The coverage area of CP by Rogers' method is less than that by Steiner's method, due to more stringent constraints for the former. The insufficient samples of CP hinder us to perform secondary classification inside CP (e.g., the subclasses of DC, MDC, MC, etc.). From this point, it seems that the latter partitioning method, adopted herein, is more applicable for the Meranti case.

At 1200 UTC 10 September (Fig. 4(a)), there are strong convective cores located on the south-east side between the radii of 60 and 120 km. After 12 h, RI begins (Fig. 4(d)). The inner-core convection increases significantly, and then a closed convection ring forms (Fig. 4(g)). Comparison of Figs. 4(b), 4(e) and 4(h) with Figs. 4(a), 4(d) and 4(g) reveals that the convective-stratiform partitioning method separates the convective and stratiform components reasonably well, distinguishing them by the dominance of high reflectivity in the CP regions. It seems that the partitioning methods employed here separate the various modes of precipitation effectively. Furthermore, the convections in the inner-core region are dominated by stratiform precipitation (SP) (Fig. 4(e)), and then turn into another mode, i.e., dominated by CP (Fig. 4(h)). This alternating distribution pattern is an interesting phenomenon during the earlier stages of RI. As for the inner-core CP, it is dominated by DC prior to RI. Then, it experiences conversion from MC + MDC (Fig. 4(f)) to MDC + DC (Fig. 4(i)) during the transition stage between RI onset and RI. Note that a large amount of inner-core DCs inside CP

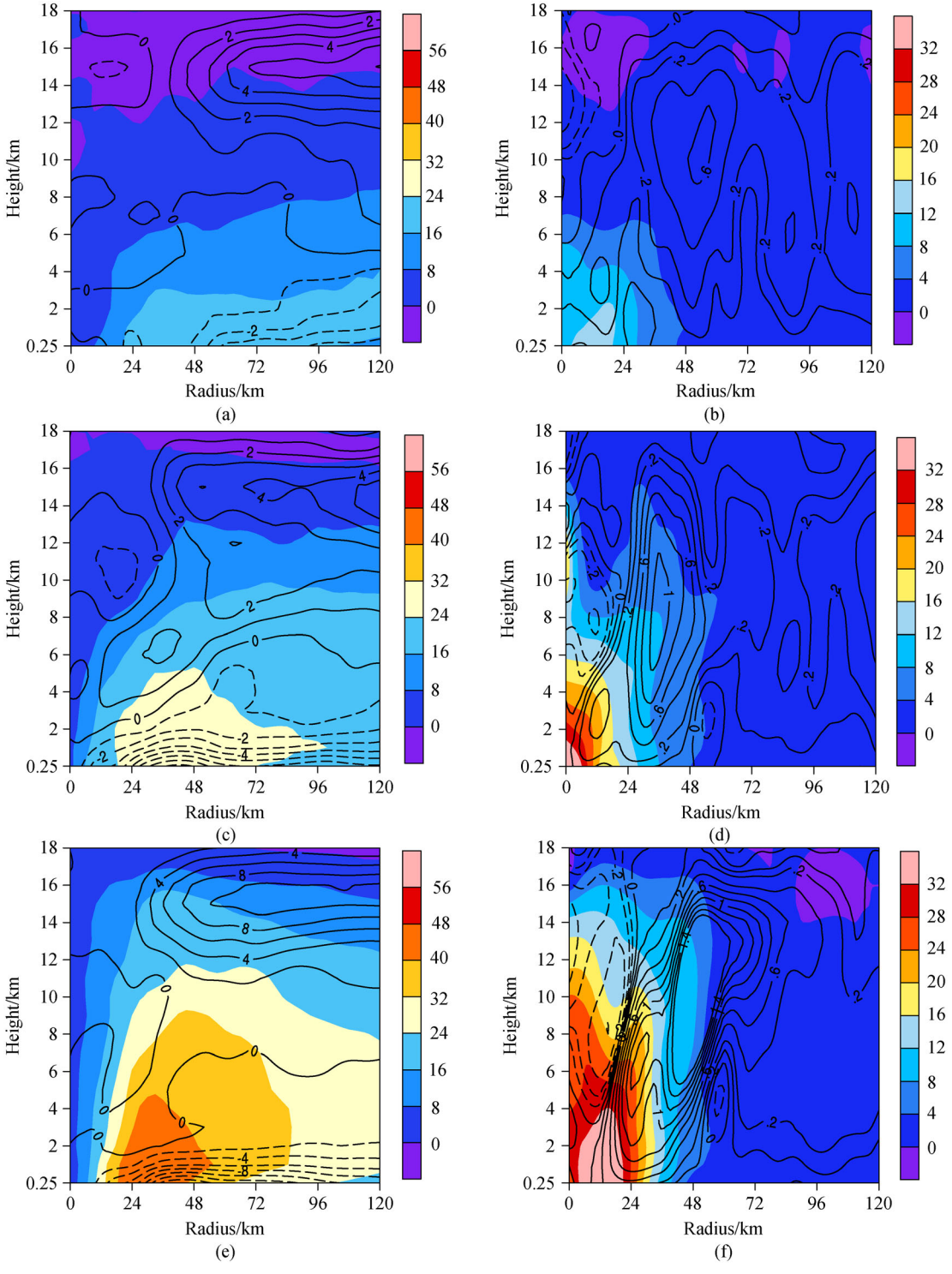

Fig. 2 Radius-height plots of azimuthally averaged (a) tangential (shaded) and radial (contoured) winds (m/s) and (b) relative vorticity (shaded, 10^{-4} m/s) and vertical velocity (contoured, m/s) at 1200 UTC 10 September 2016. (c, d) As in (a, b) but at 0000 UTC 11 September. (e, f) As in (a, b) but at 1200 UTC 11 September 2016.

regions in the south-east of the center of the typhoon is apparent in Fig. 4(c) (during the pre-RI stage) — more than that at the onset time of RI — and this is not an exception, being consistent with several previous studies (e.g., Figs. 3 (a) and 3(c) in Chen and Zhang (2013), and Fig. 13 in Wang and Wang (2014)). As for the growth of DCs within the radius of 120–180 km apparent in Fig. 4(f), this might be related to the redevelopment of the outer spiral rainbands (indicated by a strong signal of reflectivity in the same radius range) apparent in Fig. 4(d). It is the

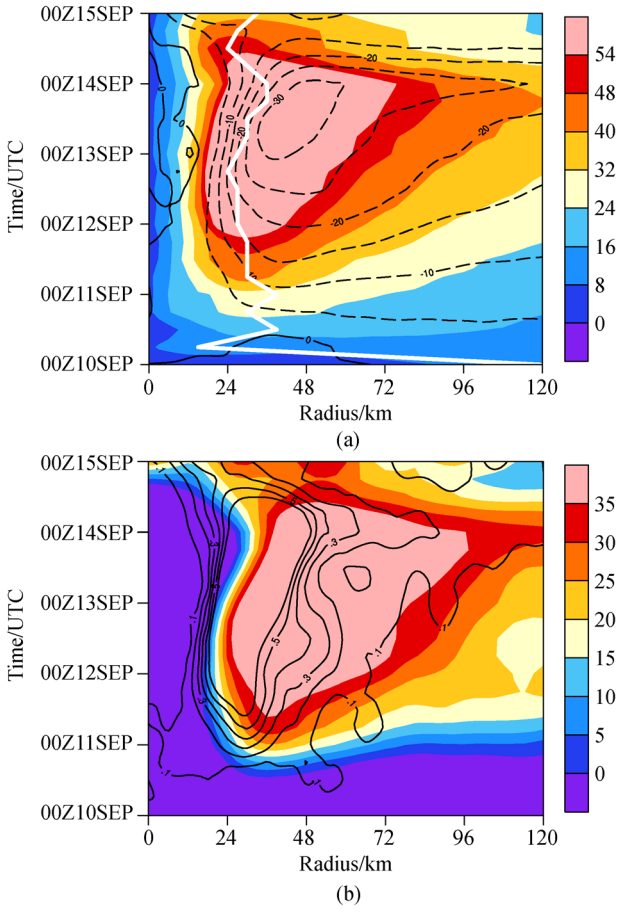

Fig. 3 Time-radius Hovmöller plots of axisymmetric (a) tangential (shaded, m/s) and radial (contoured, m/s) winds in the 0.25-km layer and (b) reflectivity (shaded, dBZ) at 3-km altitude and vertical velocity (contoured, m/s) averaged in the 0.25-km, 1-km and 2-km layers. The white curve in (a) denotes the radius of maximum wind.

coactions of high SST, high humidity, and moderately low wind shear that promote the outer strong echo and DC within echo region (Sun et al., 2013).

5 Evolutions of convections and the warm core

To investigate the RI precursors in terms of the various modes of precipitation, a time series of the numbers of convective and stratiform grid points within the inner core is shown in Fig. 5(a). The majority of members are either CP or SP, totalling on average between 70% and 90%, but dominated by the latter during the transition stage from pre-RI to RI. After 12 h of RI, the SP number decreases, while the CP elements increase gradually. The mode-trend transformation between CP and SP occurs, with the CP dominating the total. Through close inspection of the CP (Fig. 5(b)), we can see that the number of DCs is twice as high as those of the other three types prior to 6 h of RI, and then declines up until the beginning of RI. During this period, MC increases rapidly and reaches its maximum at the onset of RI. During RI, the trends of DC and MDC are almost opposite in phase, while MC shows little variation — similar to the results presented in Chen et al. (2018). Intuitively, DC and MDC (black and purple curves in Fig. 5(b)) constitute the majority of CP (red curve in Fig. 5(b)). Once the MDC develops into DC, this implies that MDC has declined, since the total sample size is invariant over a short, almost instantaneous, period of time. This is easy to follow because the total is almost invariant at a certain time, with a decrease in one component leading to an increase in the other component. As for the underlying reasons, available total energy (ATE) and its release might be a possible explanation. Also, for a short time, the ATE is almost invariant. If the ATE is consumed to feed MDC, it will provide less energy for DC growth, and vice versa.

By quantifying the hydrostatic pressure decline induced by the warming core (Hirschberg and Fritsch, 1993; Zhang and Chen, 2012), we can establish the link between the various convections and RI of the TC. The time-height cross-section of temperature perturbation (T′, shaded) is shown in Fig. 6(a), superposed with θ (contoured at intervals of 10 K), where T′ is defined with respect to the (540 km × 540 km) area-averaged temperature at 0600 UTC 10 September ($\overline{T}$). Time series of minimum pressure drops (P') reproduced from the 115-h prediction (black line in Fig. 6(b)) are also shown. Note that P' is estimated from the warm column above/beneath the θ = 370 K surface (red/blue line).

From Fig. 6(a), the warm-core structure is clear, with the upper-level core larger than 18 K at the height of 15 km. However, the mid-low-level warming begins first, before the RI of the TC (> 2 K, 5~6 km). Because the diabatic heating from different convections contributes to the warm core at distinct altitudes, the θ = 370 K surface is used to separate the contributions of the warming from different origins to the time series of P', to demonstrate this point. Therefore, the total hydrostatic pressure decline is determined by the mid-low-level warm anomaly before RI. Accompanying the onset of RI, the heating efficiency of the upper-level warm core rises swiftly (to −75 hPa, red curve in Fig. 6(b)), overruns that of the mid-low-level warm anomaly (−15 hPa), and dominates the total pressure decline (−100 hPa), accounting for the RI of the TC. That the mode takes a turn might be a predictive signal of the onset of RI. Relatively, the mid-low-level warming keeps acting on the TC's intensification slowly, maintaining a smooth and steady pressure change.

6 Local heat budgets

6.1 Potential temperature budget equation

Referring to Stern and Zhang (2013), the θ budget equation (Eq. (1)) is utilized to calculate the heating

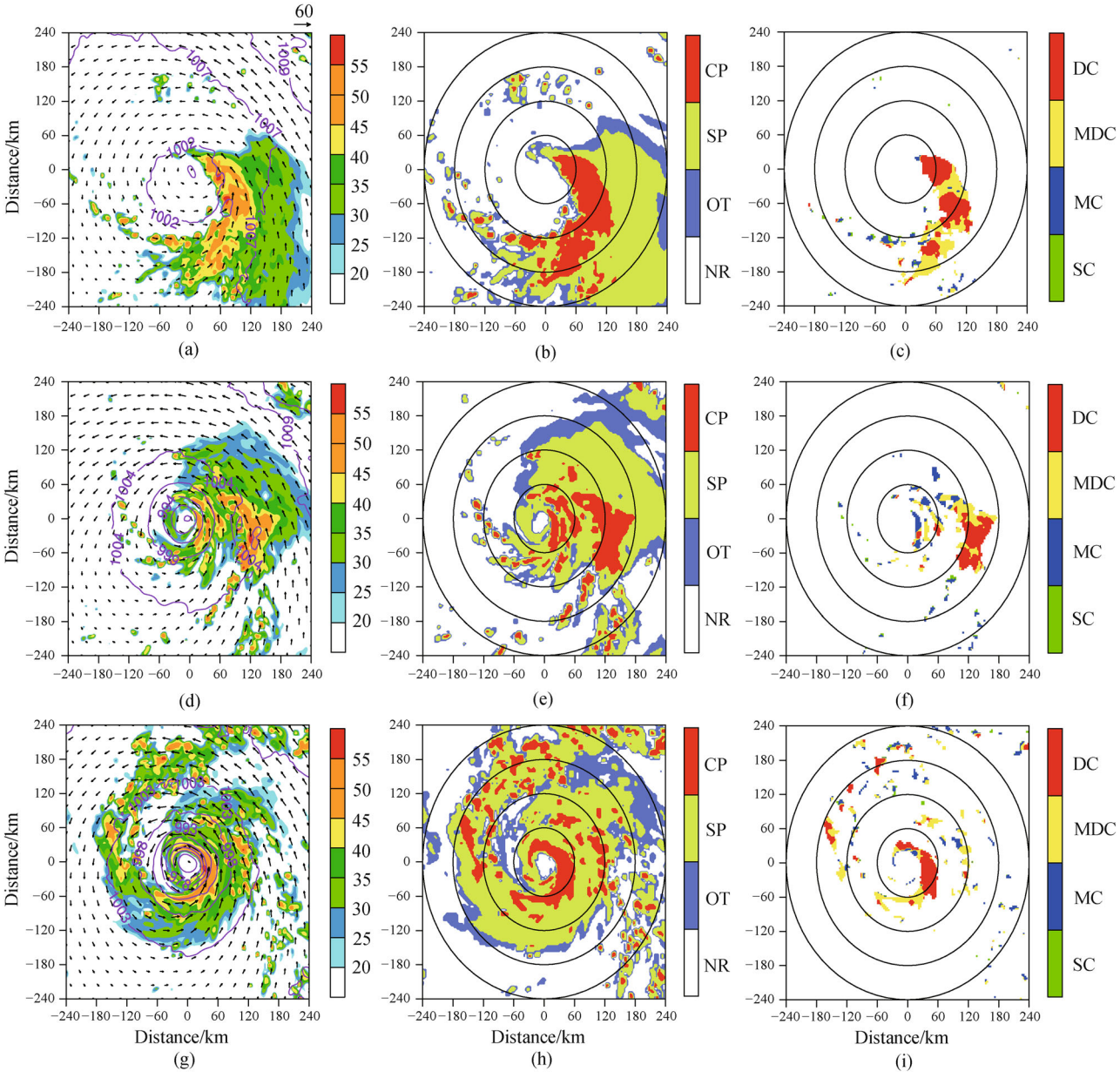

Fig. 4 (a) Simulated radar reflectivity (shaded, dBZ) at 3-km altitude and sea level pressure (isolines, hPa). (b) Results of the convective-stratiform partitioning method. (c) Results of partitioning the various types of convections (shading) at 1200 UTC 10 September. (d–f, g–i) As in (a–c) but at 0000 UTC 11 and 1200 UTC 11 September 2016, respectively.

contributions of various convections to the warm-core formation during the RI of the TC:

$$\frac{\partial\overline{\theta}}{\partial t} = -\overline{u}\frac{\partial\overline{\theta}}{\partial r} - \left(\frac{\partial\overline{u'\theta'}}{\partial r} + \frac{\overline{u'\theta'}}{r}\right) - \overline{w}\frac{\partial\overline{\theta}}{\partial z} - \frac{\partial\overline{w'\theta'}}{\partial z} + \overline{\dot{\theta}}, \tag{1}$$

where an overbar and a prime denote the azimuthal-mean and eddy component of any variable, respectively; the term $\frac{\partial\overline{\theta}}{\partial r}$ is the azimuthal-mean θ tendency; the term $-\overline{u}\frac{\partial\overline{\theta}}{\partial r}$ represents the θ tendency due to the azimuthal-mean radial θ advection (RADVM); and $-\left(\frac{\partial\overline{u'\theta'}}{\partial r} + \frac{\overline{u'\theta'}}{r}\right)$ is the θ tendency due to the eddy component of radial θ advection (RADVE). For the vertical advection terms, $-\overline{w}\frac{\partial\overline{\theta}}{\partial z}$ denotes the θ tendency from the azimuthal-mean vertical θ advection (VADVM), and $-\frac{\partial\overline{w'\theta'}}{\partial z}$ represents the θ tendency caused by the eddy component of vertical θ

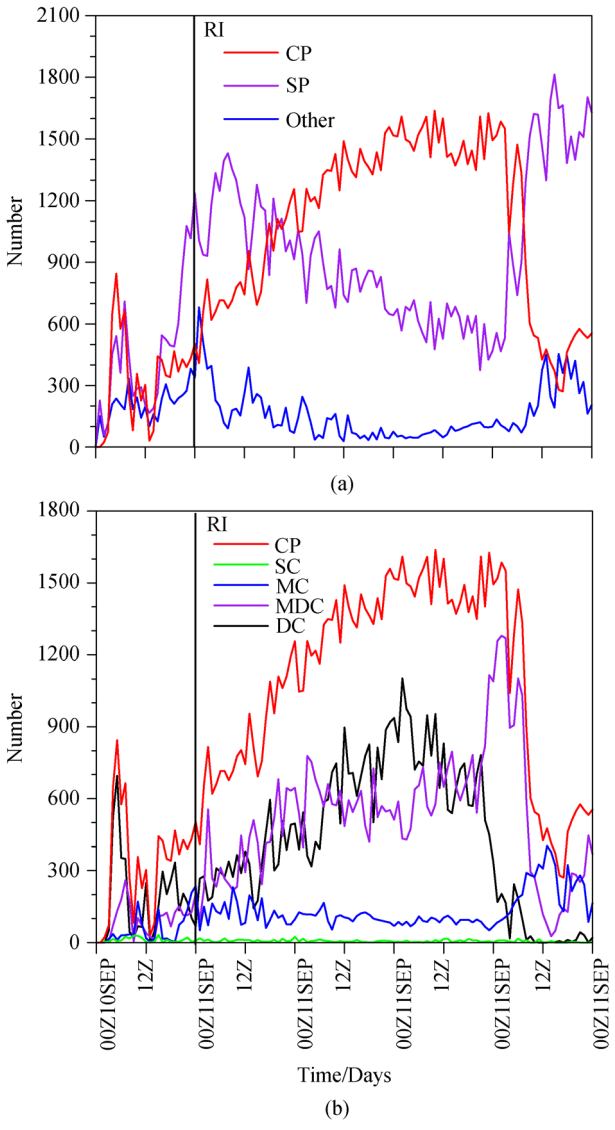

Fig. 5 Evolutions of inner-core (a) convective-precipitation (CP, red) and stratiform-precipitation (SP, purple) numbers, and (b) shallow convection (SC, green), moderate convection (MC, blue), moderate-deep convection (MDC, purple), and deep convection (DC, black) numbers.

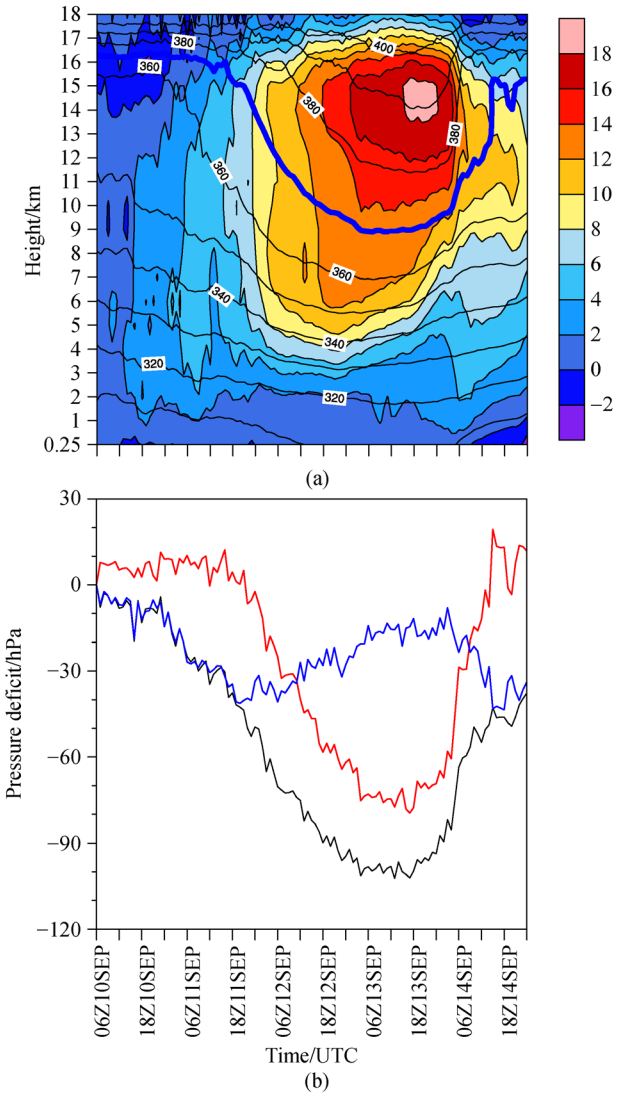

Fig. 6 (a) Time-height cross section of temperature changes (T′, shaded), superposed with potential temperature (θ, contoured at intervals of 10 K), where T′ is defined with respect to the (540 km × 540 km) area-averaged temperatures at 0600 UTC 10 September ($\overline{T}$). (b) Time series of minimum pressure drops (P') reproduced from the 66-h prediction (black line), P' estimated from the warm column above the θ = 370 K surface (red line), and from the warm column beneath the θ = 370 K surface (blue line), where P' is defined with respect to the minimum pressure at 0600 UTC 10 September.

advection (VADVE). The last term $\overline{\dot{\theta}}$ is the heating effect, including the model-output microphysics latent heat and θ tendency due to the effects of radiation and PBL parameterization. These terms are derived from the minute-level output of the numerical simulation under the height-coordinate framework.

6.2 Potential temperature budget of the total convections

For the period 2203 UTC 10 September to 1100 UTC 11 September, we examine the heat budget for this event (Fig. 7). We can see that the estimated and actual change agree well qualitatively and quantitatively, as shown in Figs. 7(a) and 7(b). However, it is worth noting that Fig. 7(b) shows a negative local theta tendency in eye region from Z = 5 km to 17 km about 5-km radially relative to the TC center. Figures 7(a) and 6(a) show a warming tendency between 9 km and 11 km in eye, which is not completely consistent with Fig. 7(b). As for the difference, possibly, the budget errors might increase during weak stages (the asymmetric structures) of TC. The local heating tendency is obvious within the radius of 30 km (Fig. 7(b)), contributing to the warm core. Two main terms are

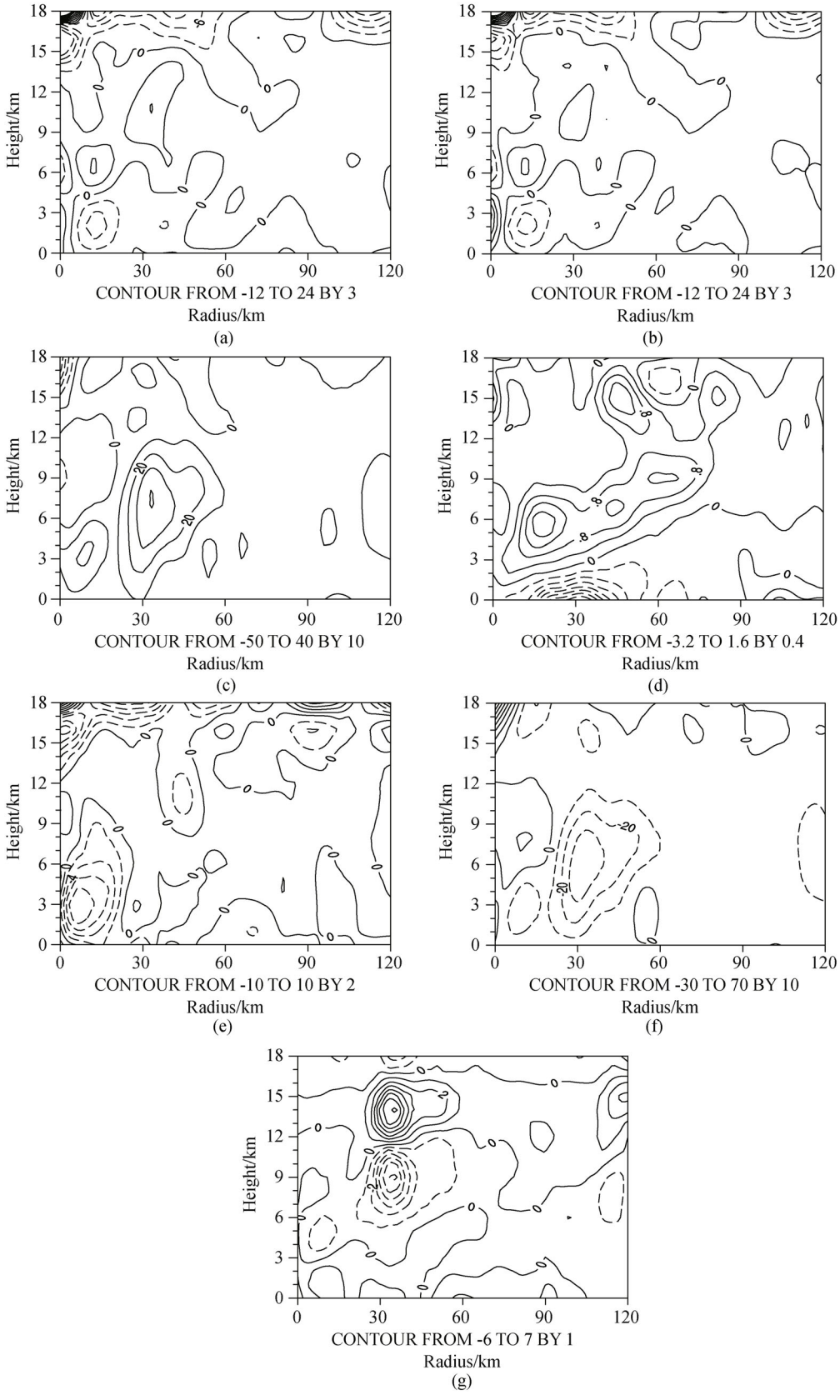

Fig. 7 Integrated (from 2203 UTC 10 September to 0000 UTC 11 September) local heat budget for this TC case in the radius-height domain: (a) actual $\overline{\Delta\theta}$ in the WRF model; (b) estimated $\overline{\Delta\theta}$ (summation of right-hand-side terms of Eq. (2)); (c) $\int_{2203\text{UTC10}}^{0000\text{UTC11}} \overline{\theta} dt$; (d) $\int_{2203\text{UTC10}}^{0000\text{UTC11}} -\overline{u}\partial\overline{\theta}/\partial r dt$; (e) $\int_{2203\text{UTC10}}^{0000\text{UTC11}} -\partial\overline{u'\theta'}/\partial r - \overline{u'\theta'}/r dt$; (f) $\int_{2203\text{UTC10}}^{0000\text{UTC11}} -\overline{w}\partial\overline{\theta}/\partial r \partial t$; (g) $\int_{2203\text{UTC10}}^{0000\text{UTC11}} -\partial w'\theta'/\partial z \partial t$. The contour intervals are 3 K in (a, b), 10 K in (c, f), and 0.4 K, 2 K and 1 K in (d), (e) and (g), respectively. Negative values are denoted by dashed contours.

responsible for the heating tendency — namely, the mean diabatic heating and the mean vertical heat advection (VADVM), shown in Figs. 7(c) and 7(f). It is worth noting that the VADVM located between the radii of 15 and 60 km is actually negative (cooling tendency) from the height of 1 to 12 km, which means that there is actually mean ascent since increases with height. However, the VADVM is positive (heating tendency) in the middle and upper troposphere within a radius of 10 km. The upper-level warming is over the eyewall region (Fig. 7(a)), while the middle-level warming is near the TC center. The upper-level warming is mainly caused by the diabatic heating of the convective eyewall (Fig. 7(c)). However, the middle-level warming near the eye region is caused by the positive VADVM due to downdrafts with adiabatic warming above the eye region (Fig. 7(f)), and the downward-tilted distribution of the RADVM (Fig. 7(d)). Relatively, as for VADVM and RADVM, the azimuthal-mean vertical advection due to downdrafts makes a larger contribution to the warm core and therefore to the deepening of the central pressure, because of the larger magnitude and closer proximity to the TC eye region (cf. Figs. 7(d) and 7 (f)). Comparatively, RADVE and VADVE can be neglected as they are too small

During 1603–1800 UTC 13 September (Fig. 8), the heat budget of this event shows the occurrence of significant warming. Peak warming of 2.5 K occurs at mid-upper levels in the core region, and there is a broad area of warming within a radius of $\leqslant$20 km from the event center (Fig. 8(b)). The duties and responsibilities of the terms in the heat budget equation are similar to those in Fig. 7. The mean diabatic heating (Fig. 8(c)) is the largest heating source, the mean vertical heat advection (VADVM) controls the vertical transport (Fig. 8(f)), and the RADVM term (Fig. 8(d)) radially transports heat from the upper to lower level in a slantwise direction. Aside from those terms, RADVE also plays a positive role in the warming of the core (Fig. 8(e)), which enhances the centripetal transport effect and accelerates the RI of the TC.

6.3 Potential temperature budget of various convections

Figure 9 shows the azimuthal-mean θ tendency. From 2203 UTC 10 September to 0000 UTC 11 September (Fig. 9(a)), there is a middle-upper level warming center at a radius of 15 km, and an upper-level warming center at a radius of 30 km. The main contribution of the middle-upper level warming core is from SP (Fig. 9(e)), and the upper-level warming core is mainly contributed by CP. The contribution of SP, however, cannot be ignored (Fig. 9(c)). From 1603 to 1800 UTC 13 September (Fig. 9(b)), the heat budget of this event shows that peak warming occurs at mid-upper levels in the core region. Meanwhile, a warming core located at the altitude of 10 km within the radii of 30 and 60 km, is mainly caused by CP (Fig. 9(d)). However, the contribution of SP is one of cooling (Fig. 9(f)).

To check the heating effect of SP on the warming core before RI, we examine the heat budget of SP. Heating tendencies from SP are integrated from 2203 UTC 10 September to 0000 UTC 11 September (Fig. 10), from which we can see that VADVM is responsible for the mid-level warming (Fig. 10(d)), while the diabatic heating is responsible for the upper-level warming (Fig. 10(a)). Compared with the above two effects, RADVM, RADVE and VADVE have a small effect on warming (Figs. 10(b), 10(c) and 10(f)). We also check the heating effect of CP on the warming core during RI (Fig. 11). The result shows that the heating source mainly comes from diabatic heating, while the cooling source is mainly from the VADVM, and the spatial distributions of heating and cooling are similar. According to Fig. 5(b), the quantity of SC is too small, so the heating effect of that can be ignored. Figure 12 shows the heating of DC, MDC and MC in CP. From 2203 UTC 10 September to 0000 UTC 11 September, a heating core is located in the middle and upper troposphere, between the radii of 30 km and 60 km, which is mainly caused by DC and MDC (Figs. 12(c) and 12(e)). At the same time, in the lower troposphere, there is also a heating core, which is actually caused by MC (Fig. 12(g)). From 1603 UTC to 1800 UTC 13 September, in the whole troposphere, only one heating core exists, mainly from DC and MDC (Figs. 12(d) and 12(f)). Relatively, MC has less of a heating effect (Fig. 12(h)). Therefore, the DC, MDC and MC are the main heating sources responsible for the warming of the upper-, middle-, and lower-level core of the TC, respectively.

7 Summary

By performing a set of cloud-resolving numerical simulations for Typhoon Meranti, which underwent RI, the track and intensity are reproduced well, especially in terms of the timing and rate of intensification during the process of RI. The spatial distributions and temporal evolutions of both convective-stratiform precipitation and shallow-DCs, the warming-core structure, and local heating budgets from various convections are examined before and during RI. The main results can be summarized as follows:

1) By investigating the spatial and temporal distributions of both convective-stratiform precipitation and shallow-DCs, the convections in the inner-core region are found to be dominated by SP, but then takes a turn into another mode, i.e., dominated by CP. This alternating distribution pattern is an interesting phenomenon during the earlier stages of RI. As for the inner-core CP, this is dominated by DC prior to RI. Then, it experiences conversion from MC + MDC to MDC + DC during the transition stage between RI onset and RI.

2) The evolution of the inner-core warm-core shows that the warm-core structure is clear, with the upper-level core larger than 18 K at the height of 15 km. However, the mid-low-level warming begins first, before the RI of the TC

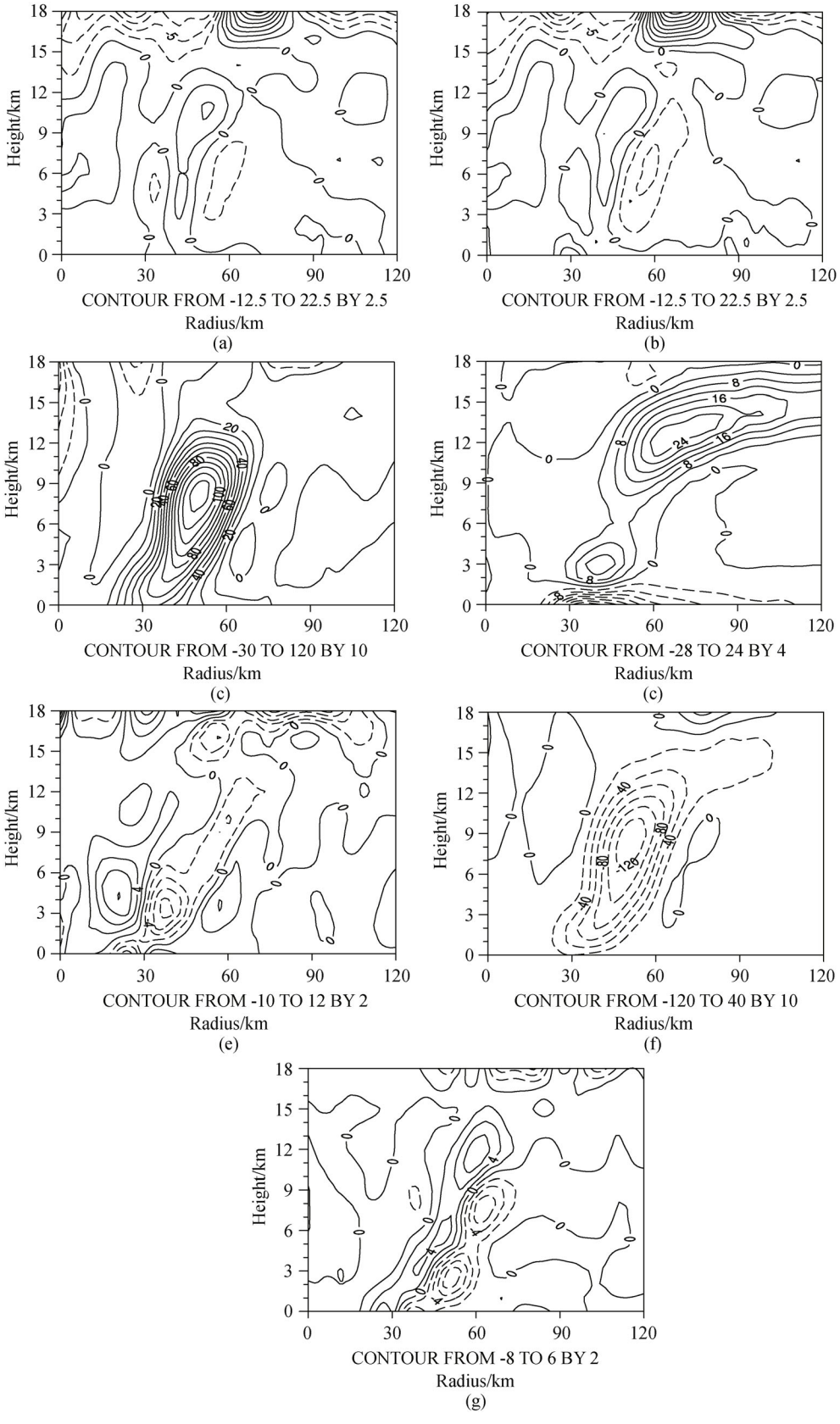

Fig. 8 As in Fig. 7 but integrated from 1603 UTC to 1800 UTC 13 September.

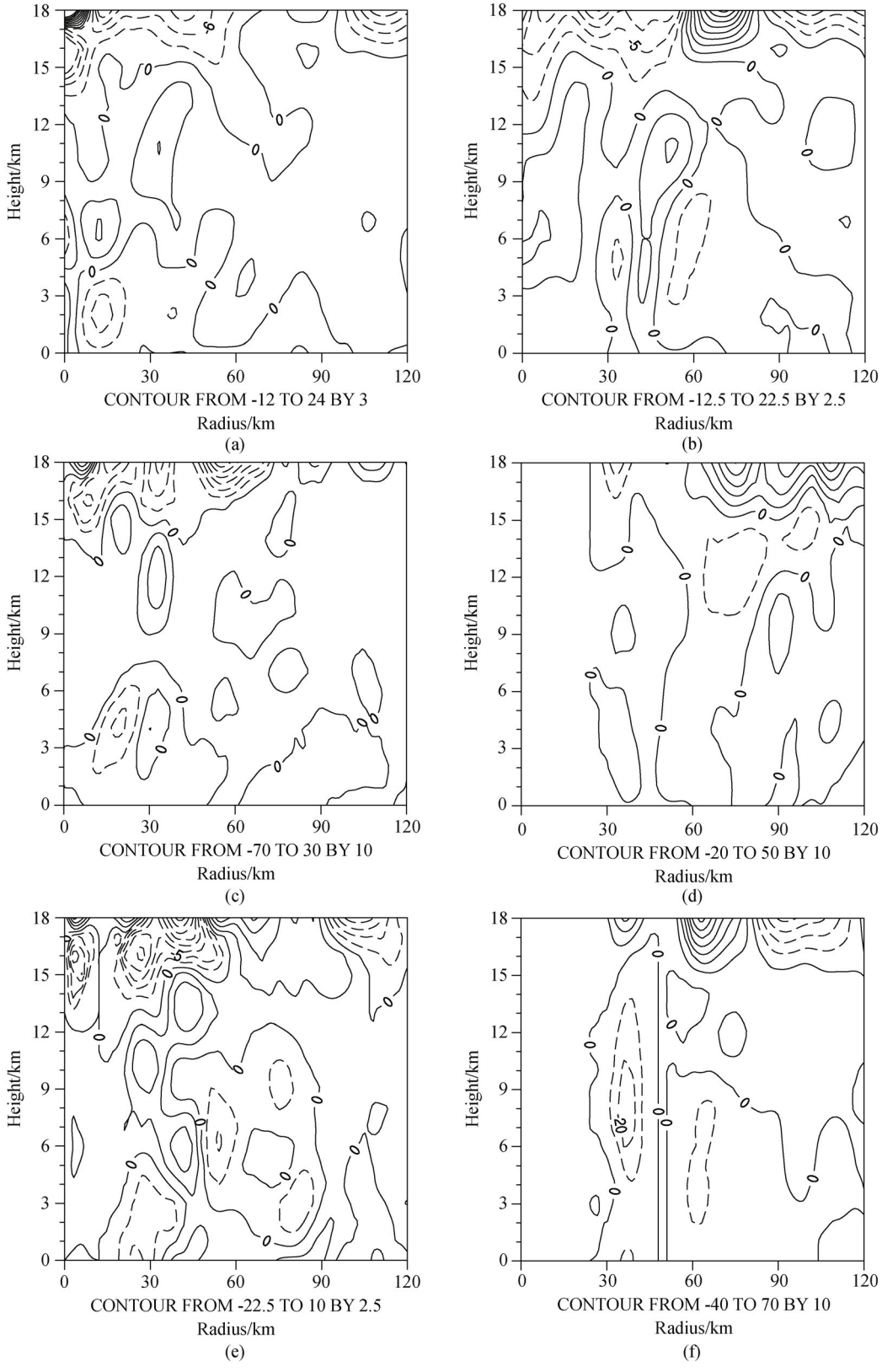

Fig. 9 Integrated local heat budget for this TC case in the radius-height domain. Heating tendencies are integrated from 2203 UTC 10 to 0000 UTC 11 September: (a) actual $\overline{\Delta\theta}$ in the WRF model; (c) convective precipitation; (e) stratiform precipitation. (b, d, f) As in (a, d, e) but from 1603 UTC to 1800 UTC 13 September.

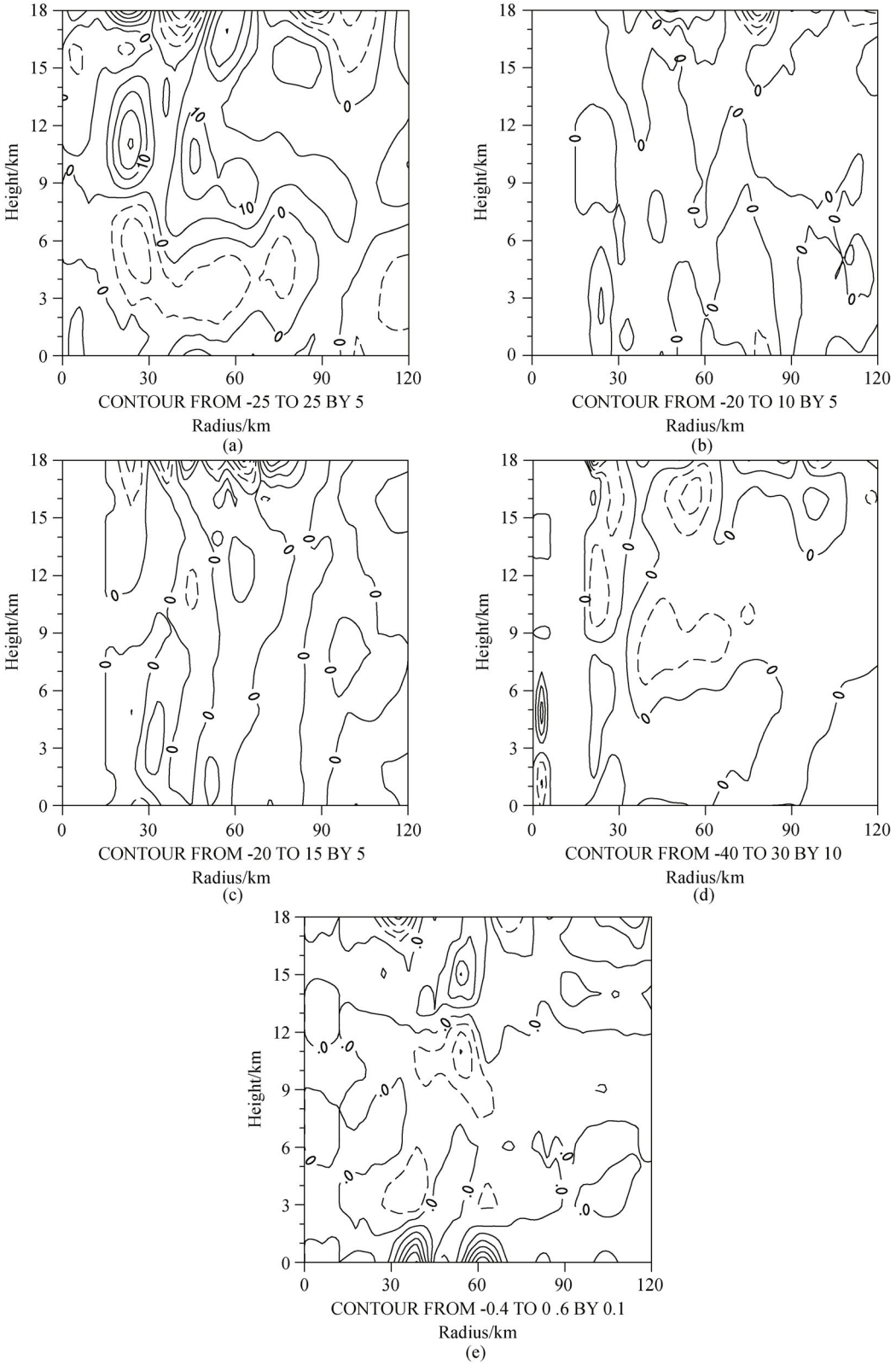

Fig. 10 Integrated local heat budget for this TC case in the radius-height domain. Heating tendencies from stratiform precipitation are integrated from 2203 UTC 10 to 0000 UTC 11 September: (a) $\int_{2203\mathrm{UTC10}}^{0000\mathrm{UTC11}} \bar{\dot{\theta}} dt$; (b) $\int_{2203\mathrm{UTC10}}^{0000\mathrm{UTC11}} -\bar{u}\partial\bar{\theta}/\partial r dt$; (c) $\int_{2203\mathrm{UTC10}}^{0000\mathrm{UTC11}} -\partial\overline{u'\theta'}/\partial r - \overline{u'\theta'}/r dt$; (d) $\int_{2203\mathrm{UTC10}}^{0000\mathrm{UTC11}} -\bar{w}\partial\bar{\theta}/\partial z \partial t$; (e) $\int_{2203\mathrm{UTC10}}^{0000\mathrm{UTC11}} -\partial\overline{w'\theta'}/\partial z \partial t$. Negative values are denoted by dashed contours.

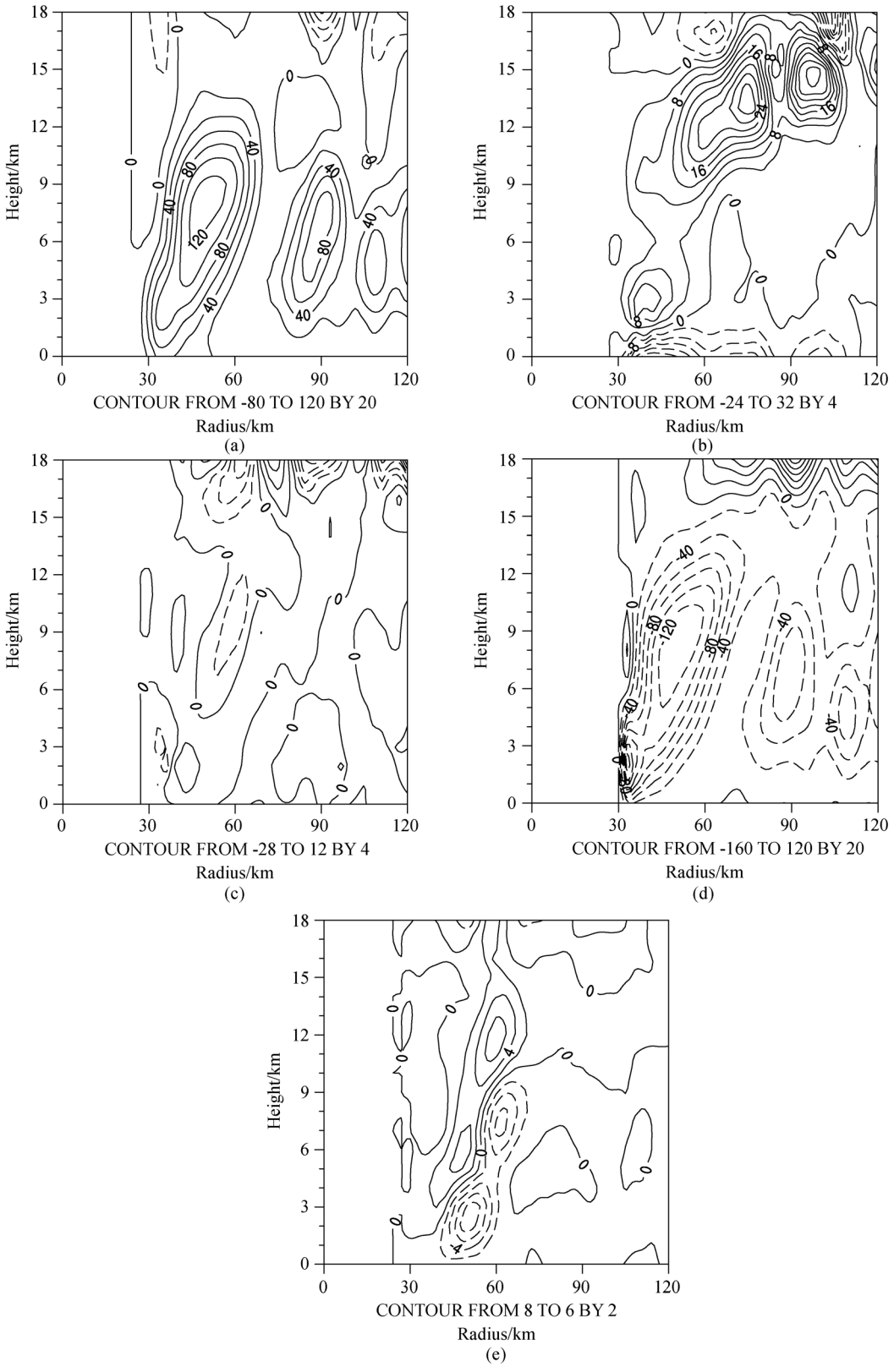

Fig. 11 As in Fig. 10 but integrated from 1603 UTC to 1800 UTC 13 September.

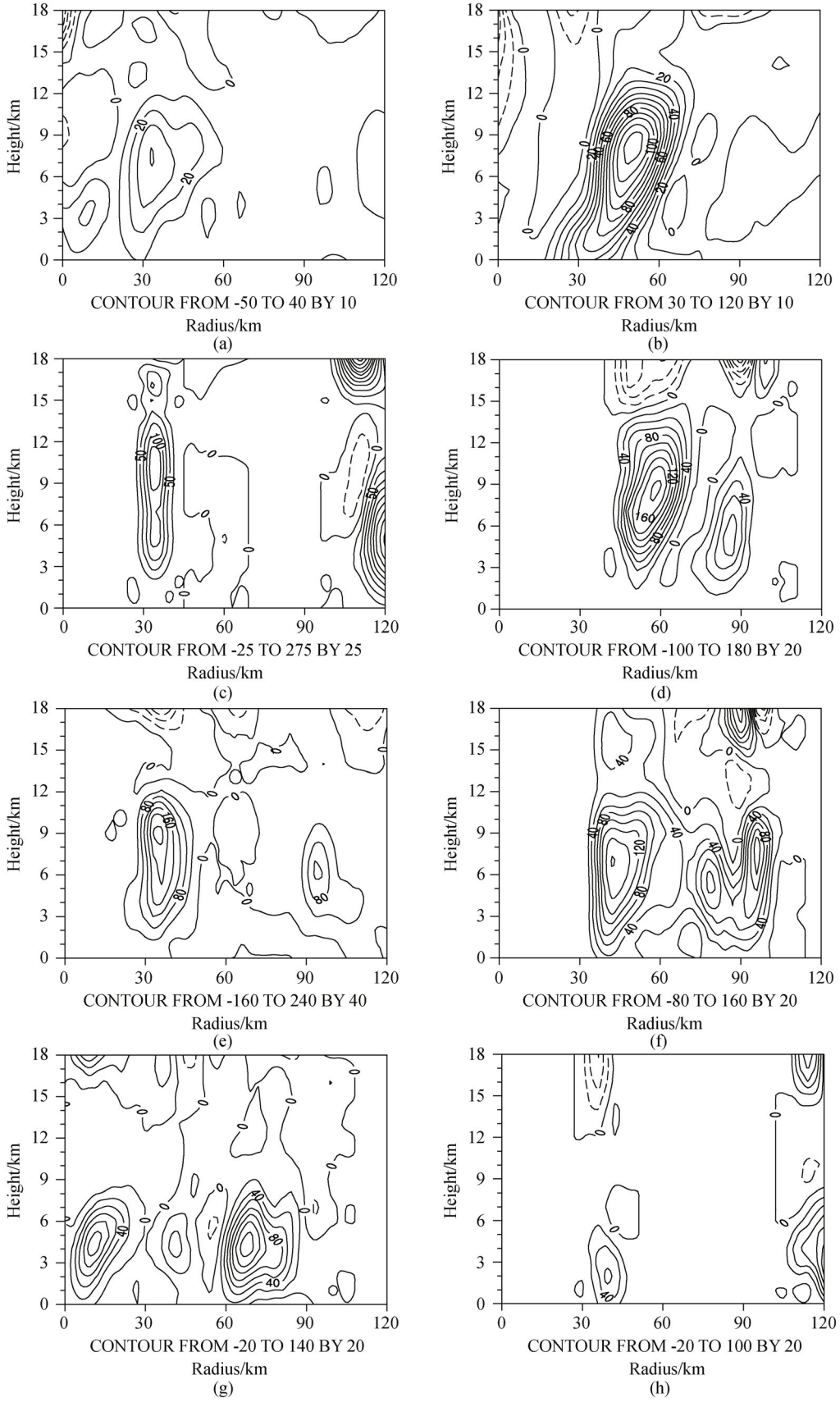

Fig. 12 Integrated local heat budget for this TC case in the radius-height domain. Diabatic heating tendencies are integrated from 2203 UTC 10 September to 0000 UTC 11 September (Left Panels): (a) total convection; (c) deep convection; (e) moderate-deep convection; (g) moderate convection. (b, d, f, h) As in (a, c, e, g) but from 1603 UTC to 1800 UTC 13 September (Right Panels).

(>2 K, 5–6 km). Because the diabatic heating from different convections contributes to the warm core at distinct altitudes, the $\theta = 370$ K surface is used to separate the contributions of the warming from different origins to the time series of P', to demonstrate this point. Therefore, the total hydrostatic pressure decline is determined by the mid-low-level warm anomaly before RI. Accompanied by the onset of RI, the heating efficiency of the upper-level warm core rises swiftly, overruns that of the mid-low-level warm anomaly, and dominates the total pressure decline, accounting for the RI of the TC.

3) Through analyses of the local θ budgets of the various convections before and during RI, the duties and responsibilities of the terms in the heat budget equation are illuminated. The azimuthal-mean diabatic heating is the largest heating source, the mean vertical heat advection controls the vertical downwards transport by adiabatic warming of compensating downdrafts above eye region, and then the radial θ advection term radially transports heat toward the center of TC in a slantwise direction. The upper-level warming is over the eyewall region, mainly caused by diabatic heating of the convective eyewall. However, the middle-level warming is near the TC center, caused by the positive VADVM due to downdrafts with adiabatic warming above the eye region, and the downward-tilted distribution of the RADVM. Relatively, as for VADVM and RADVM, the azimuthal-mean vertical θ advection due to downdrafts makes a larger contribution to the warm core and therefore to the deepening of the central pressure, because of the larger magnitude and closer proximity to the TC eye region. Those are the common characteristics for both stratiform and convective precipitation. Aside from those terms, for convective precipitation, the eddy component of radial θ advection also plays a positive role in warming the core, which enhances the centripetal transport effect and accelerates the RI process of the TC. Comprehensive analyses of the warm core and various convections shows that the DC, MDC and MC are responsible for warming the upper-, middle- and lower-level core of the TC, respectively. The heating budget calculations from the various convections co-act on Meranti together, accelerating the RI process of the TC.

Acknowledgements Very thanks for the valuable comments of the three anonymous reviewers, which helped considerably in improving the original manuscript. This work was supported by the National Key Research and Development Program of China (Grant Nos. 2018YFC1506801 and 2018YFF0300102), the Plateau Atmosphere and Environment Key Laboratory of Sichuan Province (Grant No. PAEKL-2017-K3), and the National Natural Science Foundation of China (Grant Nos. 41405059, 41575064, 41875079, 41875077, 41575093, and 41630532).

References

Chen H, Zhang D L (2013). On the rapid intensification of Hurricane Wilma (2005). Part II: convective bursts and the upper-level warm core. J Atmos Sci, 70(1): 146–162

Chen X M, Xue M, Fang J (2018). Rapid intensification of Typhoon Mujigae (2015) under different sea surface temperatures: structural changes leading to rapid intensification. J Atmos Sci, 75(12): 4313–4335

CMA (2016). Member Report: China. ESCAP/WMO Typhoon Committee: 9–14

DeMaria M, Sampson C R, Knaff J A, Musgrave K D (2014). Is tropical cyclone intensity guidance improving? Bull Am Meteorol Soc, 95(3): 387–398

Guimond S R, Heymsfield G M, Turk F J (2010). Multiscale observations of hurricane Dennis (2005): the effects of hot towers on rapid intensification. J Atmos Sci, 67(3): 633–654

Han B, Fan J, Varble A, Morrison H, Williams C R, Chen B, Dong X, Giangrande S E, Khain A, Mansell E, Milbrandt J A, Shpund J, Thompson G (2019). Cloud-resolving model intercomparison of an MC3E squall line case. Part II: stratiform precipitation properties. J Geophys Res D Atmospheres, 124(2): 1090–1117

Hendricks D A, Peng M S, Fu B, Li T (2010). Quantifying environmental control on tropical cyclone intensity change. Mon Weather Rev, 138(8): 3243–3271

Heymsfield G M, Halverson J B, Simpson J, Tian L, Bui T P (2001). ER-2 Doppler radar investigations of the eyewall of Hurricane Bonnie during the convection and moisture Experiment-3. J Appl Meteorol, 40(8): 1310–1330

Hirschberg P A, Fritsch J M (1993). On understanding height tendency. Mon Weather Rev, 121(9): 2646–2661

Huang Y, Wang Y, Cui X (2019). Differences between convective and dtratiform precipitation budgets in a torrential rainfall event. Adv Atmos Sci, 36(5): 495–509

Kaplan J, DeMaria M (2003). Large-scale characteristics of rapidly intensifying tropical cyclones in the North Atlantic basin. Weather Forecast, 18(6): 1093–1108

Li M X, Ping F, Tang X B, Yang S (2019). Effects of microphysical processes on the rapid intensification of Super-Typhoon Meranti. Atmos Res, 219: 77–94

Li Q Q, Wang Y Q (2012). A comparison of inner and outer spiral rainbands in a numerically simulated tropical cyclone. Mon Weather Rev, 140(9): 2782–2805

Lin I I, Wu C C, Pun I F, Ko D S (2008). Upper-ocean thermal structure and the western North Pacific category 5 typhoons. Part I: ocean features and the category 5 typhoons' intensification. Mon Weather Rev, 136(9): 3288–3306

Marks F D, Shay L K (1998). Landfalling tropical cyclones: forecast problems and associated research opportunities. Bull Am Meteorol Soc,79(2): 305–323

Molinari J, Vollaro D (2010). Rapid intensification of a sheared tropical storm. Mon Weather Rev, 138(10): 3869–3885

Nguyen L T, Molinari J (2012). Rapid intensification of a sheared, fast-moving hurricane over the Gulf Stream. Mon Weather Rev, 140(10): 3361–3378

Reasor P D, Eastin M D, Gamache J F (2009). Rapidly intensifying Hurricane Guillermo (1997). Part I: low-wavenumber structure and evolution. Mon Weather Rev, 137(2): 603–631

Rogers R (2010). Convective-scale structure and evolution during a high-resolution simulation of tropical cyclone rapid intensification. J

Atmos Sci, 67(1): 44–70

Rogers R F, Reasor P D, Zhang J A (2015). Multiscale structure and evolution of Hurricane Earl (2010) during rapid intensification. Mon Weather Rev, 143(2): 536–562

Steiner M, Houze R A Jr, Yuter S E (1995). Climatological characterization of three-dimensional storm structure from operational radar and rain gauge data. J Appl Meteorol, 34(9): 1978–2007

Stern D P, Zhang F Q (2013). How does the eye warm? Part I: a potential temperature budget analysis of an idealized tropical cyclone. J Atmos Sci, 70(1): 73–90

Sun Y Q, Jiang Y X, Tan B, Zhang F Q (2013). The governing dynamics of the secondary eyewall formation of Typhoon Sinlaku (2008). J Atmos Sci, 70(12): 3818–3837

Tao C, Jiang H (2015). Distributions of shallow to very deep precipitation-convection in rapidly intensifying tropical cyclones. J Clim, 28(22): 8791–8824

Wang H, Wang Y Q (2014). Full access a numerical study of Typhoon Megi (2010). Part I: rapid intensification. Mon Weather Rev, 142(1): 29–48

Wang Y Q (2009). How do outer spiral rainbands affect tropical cyclone structure and intensity? J Atmos Sci, 66(5): 1250–1273

Wang Y, Wu C C (2004). Current understanding of tropical cyclone structure and intensity changes—a review. Meteor Atmos Phys, 87 (4): 257–278

Zhang D L, Chen H (2012). Importance of the upper-level warm core in the rapid intensification of a tropical cyclone. Geophys Res Lett, 39 (2): L02806

Zheng Y, Gong Y, Chen J, Tian F (2019). Warm-season diurnal variations of total, stratiform, convective, and extreme hourly precipitation over central and eastern China. Adv Atmos Sci, 36(2): 143–159